
Not All Tasks Quantize Equally: Fisher-Guided Quantization for Visual Geometry Transformer

Yipu Zhang^{1,†} Jintao Cheng^{1,†} Weilun Feng^{2,3,†} Jiehao Luo⁴
Chuangang Yang² Zhulin An² Yongjun Xu^{2,5} Wei Zhang^{1,*}

¹Department of Electronic and Computer Engineering, HKUST

²State Key Laboratory of AI Safety, Institute of Computing Technology,
Chinese Academy of Sciences

³University of Chinese Academy of Sciences

⁴School of Data Science and Engineering, South China Normal University

⁵Xiamen Institute of Data Intelligence

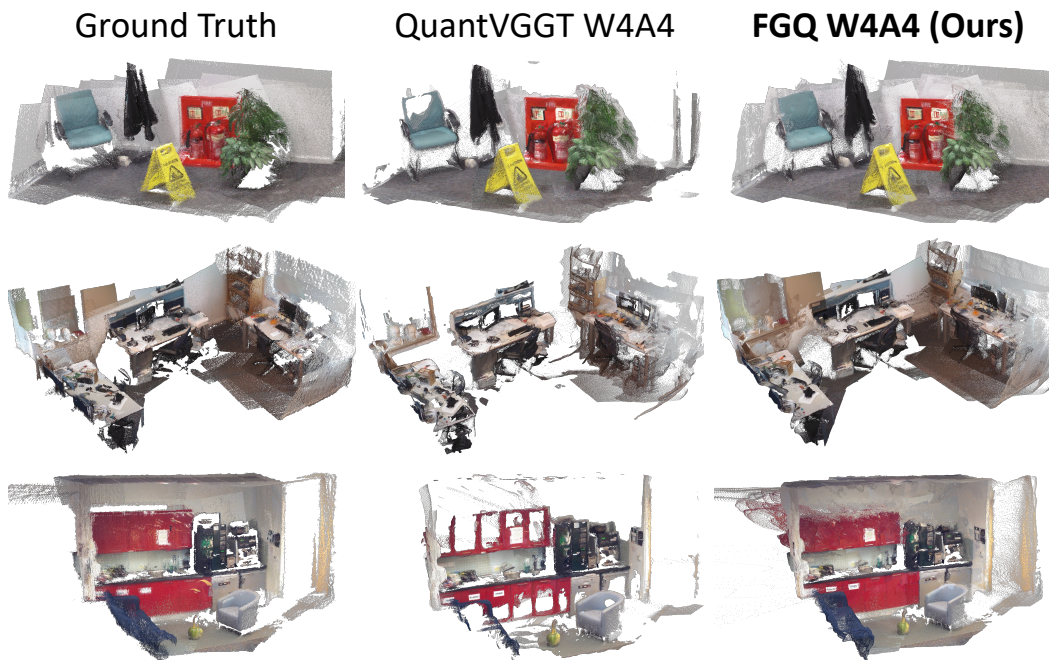


Figure 1: **FGQ** effectively preserves the point map reconstruction fidelity under 4-bit quantization, surpassing previous state-of-the-art VGGT (QuantVGGT [Feng et al., 2025]) quantization.

Abstract

Feed-forward 3D reconstruction models, represented by Visual Geometry Grounded Transformer (VGGT), jointly predict multiple visual geometry tasks such as depth estimation, camera pose prediction, and point map reconstruction in a single forward pass. They have been widely adopted in 3D vision applications, but their billion-scale parameters bring substantial memory and computation overhead, posing challenges for on-device deployment. Post-Training Quantization

[†]Equal contribution.

^{*}Corresponding author: Wei Zhang <wei.zhang@ust.hk>.

(PTQ) is an effective technique to reduce this overhead. Existing PTQ methods for feed-forward 3D models mainly focus on handling heavy-tailed activation distributions and constructing diverse calibration datasets. However, we observe that feed-forward 3D models predict multiple geometric attributes through a shared backbone, where different transformer blocks and hidden channels contribute distinctly to each task, resulting in substantially different sensitivities to quantization errors across tasks, blocks, and channels. Consequently, treating all tasks equally over-emphasizes insensitive tasks and causes significant accuracy loss on the sensitive ones. To address this issue, we propose Fisher-Guided Quantization (**FGQ**) for feed-forward 3D reconstruction models. Specifically, **FGQ** uses the diagonal Fisher information matrix to quantify the different sensitivities across tasks, blocks, and channels, and incorporates these sensitivities into the Learnable Affine Transformation during calibration to better preserve the channels and blocks most critical to each task. Extensive experiments across camera pose estimation, point map reconstruction, and depth estimation show that **FGQ** consistently outperforms state-of-the-art quantization baselines on VGGT, achieving up to 39% relative improvement under the 4-bit quantization. Code will be available after acceptance.

1 Introduction

Feed-forward 3D reconstruction methods, represented by Visual Geometry Grounded Transformer (VGGT) [Wang et al., 2025a], have achieved significant progress by jointly predicting depth, camera poses, and point maps in a single forward pass. They have been widely adopted in downstream applications such as spatial reasoning [Hu et al., 2025], robotics [Yang et al., 2026], and autonomous driving [Lin et al., 2025]. However, their billion-scale parameters introduce prohibitive computation and memory overhead during inference, limiting real-time processing and on-device deployment [Zhang et al., 2026].

A variety of methods have been proposed to address this efficiency bottleneck, including quantization [Feng et al., 2025, Zhang et al., 2026, Pan et al., 2026], token merging [Shen et al., 2025, Shu et al., 2025], and architectural modifications that redesign the attention or computation flow for better efficiency [Wang and Xu, 2025, Sun et al., 2025a].

Existing PTQ methods for feed-forward 3D models primarily address two challenges: (i) mitigating activation outliers associated with special tokens (e.g., camera and register tokens), and (ii) capturing the geometric and semantic complexity of 3D representations during calibration dataset construction. However, these approaches overlook a critical characteristic of these models: their inherent multi-task architecture. Since depth, pose, and point map prediction operate at vastly different scales and are evaluated with distinct metrics, they exhibit markedly different sensitivities to quantization-induced perturbations. As illustrated in Fig. 2, applying a uniform quantization strategy causes disproportionately severe degradation in point map reconstruction compared to camera pose and depth estimation. Beyond this task-level disparity, Fig. 3 (a)&(b) further shows that the per-block and per-channel quantization loss follows markedly different patterns across tasks. Together, these observations confirm that different transformer blocks and hidden channels contribute distinctly to each task, leading to substantially different quantization sensitivities across tasks, blocks, and channels.

To this end, we propose Fisher-Guided Quantization (**FGQ**), a task-aware PTQ framework for feed-forward 3D reconstruction models. **FGQ** leverages the diagonal Fisher information matrix to jointly quantify quantization sensitivity across three granularities: tasks (depth, pose, and point map), transformer blocks, and hidden channels. These sensitivities are then incorporated into the Learnable Affine Transformation during calibration, guiding the transformation to preserve the channels and blocks most critical to each task.

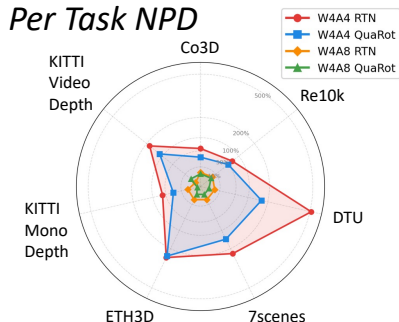


Figure 2: Normalized Performance Degradation (NPD) across various tasks.

Our contributions are summarized as follows:

- We identify the multi-task sensitivity problem in PTQ for feed-forward 3D reconstruction, showing that different transformer blocks and hidden channels contribute distinctly to each task, leading to substantially different quantization sensitivities across tasks, blocks, and channels.
- We propose Fisher-Guided Quantization (**FGQ**), which uses the diagonal Fisher information matrix to quantify per-task, per-block, and per-channel sensitivity, and integrates these sensitivities into the Learnable Affine Transformation objective to guide calibration toward the most quantization-sensitive components.
- Extensive experiments on camera pose estimation, point map reconstruction, and depth estimation demonstrate that **FGQ** improves task performance by up to 39% over state-of-the-art PTQ baselines under 4-bit quantization, with the largest gains on point map reconstruction, where prior PTQ methods incur the most significant degradation.

2 Related Work

Efficient Feed-Forward 3D Reconstruction. Recent work targets the high compute and memory cost of feed-forward 3D reconstruction models such as VGGT. Token merging methods like FastVGGT [Shen et al., 2025] and LiteVGGT [Shu et al., 2025] fuse similar tokens by exploiting redundancy in global attention. Architectural redesigns restructure attention itself: FlashVGGT [Wang and Xu, 2025] approximates global attention as cross-attention to a compact set of descriptor tokens generated by spatial resampling, while AVGGT [Sun et al., 2025a] converts early global layers into frame attention and subsamples K/V over patch tokens. Closest to our work, recent PTQ methods [Feng et al., 2025, Zhang et al., 2026] address two key challenges in quantizing these models: (i) mitigating activation outliers from data-independent special tokens (e.g., camera and register tokens), which yield heavy tails and extreme channel and token variance unfriendly to low-bit quantization; and (ii) dealing with calibration data that captures the geometric and semantic complexity of 3D multi-view inputs. However, prior PTQ methods apply uniform quantization across all heads and treat feed-forward 3D models as single-task models, overlooking the distinct quantization sensitivities of their depth, pose, and point map predictions.

Model Quantization. Post-training quantization (PTQ) reduces the memory and compute cost of large language models. Weight-only methods such as GPTQ [Frantar et al., 2022] and AWQ [Lin et al., 2024] compress weights to low bit-widths with minimal accuracy loss. To further quantize activations and the KV cache, a recent line of work applies affine transformations to suppress outliers before quantization. QuaRot [Ashkboos et al., 2024] uses fixed random Hadamard rotations, while SpinQuant [Liu et al., 2024] and FlatQuant [Sun et al., 2025b] instead learn the transformation matrices during calibration: SpinQuant optimizes rotation matrices via Cayley optimization, and FlatQuant learns lightweight per-layer affine transformations that flatten weight and activation distributions. To better involve the sensitivity in the quantization process, we adopt the learnable affine transform based method as detailed in Sec. 3.2.3.

3 Method

3.1 Preliminary

Visual Geometry Grounded Transformer (VGGT) [Wang et al., 2025a] is a feed-forward transformer that maps a set of N input images $(I_i)_{i=1}^N$ to their 3D attributes (camera parameters, depth maps, point maps, and tracking features) in a single pass. Each image I_i is first patchified by a DINOv2 [Oquab et al., 2023] encoder into K tokens $t_i \in \mathbb{R}^{K \times C}$, and the full token set is denoted $\mathbf{T} = [t_1; t_2; \dots; t_N] \in \mathbb{R}^{N \times K \times C}$. The backbone consists of L *Alternating-Attention* (AA) blocks, each interleaving two self-attention operations:

$$\mathbf{T}_i^{(\ell+\frac{1}{2})} = \text{FrameAttention}(\mathbf{T}_i^{(\ell)}), \quad i = 1, \dots, N, \quad (1)$$

$$\mathbf{T}^{(\ell+1)} = \text{GlobalAttention}(\mathbf{T}^{(\ell+\frac{1}{2})}), \quad (2)$$

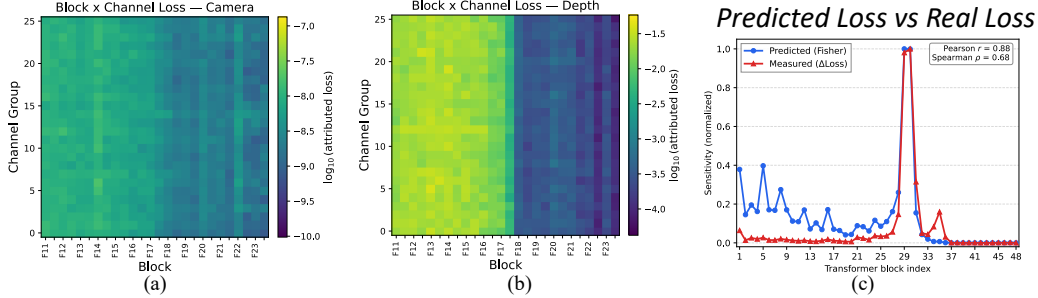


Figure 3: Fisher information accurately predicts quantization sensitivity and reveals task-specific patterns. (a) Per-block and per-channel quantization loss for camera pose estimation. (b) Per-block and per-channel quantization loss for depth estimation. The markedly quantization loss profiles between tasks motivate task-aware quantization strategies. (c) Fisher-predicted loss versus empirically measured loss across transformer blocks under W4A4 quantization, showing strong correlation ($r = 0.88$).

where $\ell \in \{0, 1, \dots, L-1\}$ indexes the AA block, $\mathbf{T}^{(\ell)}$ denotes the token state at the input of the ℓ -th block (with $\mathbf{T}^{(0)} = \mathbf{T}$), and $\mathbf{T}^{(\ell+\frac{1}{2})}$ denotes the intermediate state after frame attention but before global attention within the same block. Here, $\text{FrameAttention}(\cdot)$ operates independently within each image’s K tokens to preserve per-view structure, and $\text{GlobalAttention}(\cdot)$ operates jointly over all $N \times K$ tokens to propagate information across views. The refined tokens $\mathbf{T}^{(L)}$ are then decoded by task-specific heads into the final 3D predictions.

3.2 Fisher-Guided Quantization

3.2.1 Sensitivity Varies Across Tasks

To quantify the impact of quantization on each downstream task, we define the Normalized Performance Degradation (NPD) of task k at bit-width b as

$$\text{NPD}_k(b) = \frac{|\text{Metric}_k(b) - \text{Metric}_k(\text{FP16})|}{\text{Metric}_k(\text{FP16})} \times 100\%. \quad (3)$$

Task-level sensitivity. As shown in Fig. 2, applying W4A4 quantization to VGGT with PTQ methods leads to highly unbalanced degradation across tasks: camera pose estimation remains relatively robust, while point map reconstruction collapses with an NPD of 200% \sim 500%. This indicates that VGGT’s shared backbone routes different geometric attributes through the same parameters, yet each task tolerates quantization noise to varying degrees.

Block and channel-level sensitivity. To locate the source of this asymmetry, we measure the per-block and per-channel quantization loss separately for the camera and depth tasks. As shown in Fig. 3(a) and (b), the two tasks produce clearly different loss profiles along both dimensions: blocks and channels that are critical for one task are often unimportant for the other. As a result, a uniform quantization policy is forced to compromise between tasks, and any objective that weights all tasks equally is dominated by the insensitive ones and therefore sacrifices accuracy on the sensitive ones. These observations motivate a task-aware design that allocates precision according to the sensitivity of each task at both the block and channel level.

3.2.2 Fisher Information for Sensitivity Measurement

To realize this design, we introduce a task-aware sensitivity score at the block and channel level, which is cheap to compute and can be directly plugged into the calibration objective. We derive the score from a second-order expansion of each task loss, approximate the Hessian with the Fisher information to avoid its prohibitive cost, and further reduce it to its diagonal form for efficiency.

Quantization error and the role of the Hessian. Let $\mathbf{h}_l \in \mathbb{R}^C$ denote the output of block l , where C is the channel dimension, and let \mathcal{L}_k denote the loss of task k . Quantization perturbs \mathbf{h}_l by $\Delta\mathbf{h}_l$,

which aggregates the effect of all weight and activation rounding inside the block. A second-order Taylor expansion of \mathcal{L}_k around the full-precision output gives

$$\Delta\mathcal{L}_k \approx \mathbf{g}_k^\top \Delta\mathbf{h}_l + \frac{1}{2} \Delta\mathbf{h}_l^\top \mathbf{H}_k \Delta\mathbf{h}_l, \quad (4)$$

where \mathbf{g}_k and \mathbf{H}_k are the gradient and Hessian of \mathcal{L}_k with respect to \mathbf{h}_l . A pre-trained VGGT sits near a local optimum, and therefore $\mathbb{E}[\mathbf{g}_k] \rightarrow \mathbf{0}$ and the first-order term vanishes in expectation [LeCun et al., 1989]. The expected loss change is governed by the Hessian term,

$$\mathbb{E}[\Delta\mathcal{L}_k] \approx \frac{1}{2} \Delta\mathbf{h}_l^\top \mathbf{H}_k \Delta\mathbf{h}_l, \quad (5)$$

which assigns a task-specific cost to each direction of perturbation: directions with large eigenvalues amplify quantization error into task loss, while directions with small eigenvalues absorb it.

Fisher information as a tractable surrogate. While Eq. 5 formalizes the appropriate notion of block-wise sensitivity, direct evaluation of \mathbf{H}_k is computationally prohibitive in our setting. Second-order automatic differentiation incurs substantial runtime overhead per block and per task, and explicit storage of \mathbf{H}_k requires $\mathcal{O}(C^2)$ memory per block. To avoid these costs, we use a Fisher-based surrogate for the Hessian. This substitution is common in the pruning and quantization literature [Kwon et al., 2022, Yang et al., 2024] and is motivated by the following standard identity.

For our calibration setting, x denotes a set of input images. The variable y denotes the target signal used to compute the task loss \mathcal{L}_k . We write $q_k(x, y) = q_k(x)q_k(y | x)$ for the task-specific calibration distribution. For readability, the proposition below omits the task subscript and writes q instead of q_k .

Proposition 3.1 (Conditional Hessian–Fisher identity). *Let z be a differentiable argument of a normalized conditional model $p_z(y | x)$, where z may denote model parameters or an intermediate activation treated as a local input to the remaining network. Define the negative log-likelihood loss $\ell(z; x, y) = -\log p_z(y | x)$. Assume standard regularity conditions that allow differentiation under the integral. If, at z^* , the data conditional distribution is matched by the model, i.e., $q(y | x) = p_{z^*}(y | x)$ for $q(x)$ -almost every x , then*

$$\mathbb{E}_{x \sim q(x), y \sim q(y|x)} [\nabla_z^2 \ell(z^*; x, y)] = \mathbb{E}_{x \sim q(x), y \sim q(y|x)} [\nabla_z \ell(z^*; x, y) \nabla_z \ell(z^*; x, y)^\top]. \quad (6)$$

The matrix on the right-hand side is the Fisher information matrix with respect to z .

We give a self-contained proof of Proposition 3.1, which is an instance of the second Bartlett identity, in Appendix A. The proposition shows that, under a correctly specified likelihood and population expectation, the expected Hessian of the negative log-likelihood equals the Fisher information matrix. In practice, we use this identity as a motivation for replacing the block Hessian by an empirical Fisher estimated from first-order gradients at a well-trained checkpoint.

Instantiating this surrogate at the output of block l gives

$$\mathbb{E}[\Delta\mathcal{L}_k] \approx \frac{1}{2} \Delta\mathbf{h}_l^\top \mathbf{F}_k^{h_l} \Delta\mathbf{h}_l, \quad [\mathbf{F}_k^{h_l}]_{c,c'} = \mathbb{E}_{(x,y) \sim \mathcal{D}_{\text{cal}}} \left[\frac{\partial \mathcal{L}_k(x, y)}{\partial h_{l,c}} \frac{\partial \mathcal{L}_k(x, y)}{\partial h_{l,c'}} \right]. \quad (7)$$

Here \mathcal{D}_{cal} is a small calibration set. Since $\mathbf{F}_k^{h_l}$ only uses first-order gradients, it can be estimated with one backward pass per task. Moreover, evaluating the Fisher at the block output is convenient because $\Delta\mathbf{h}_l$ already contains the total perturbation induced by quantizing block l . Thus a single block-level Fisher term captures the joint sensitivity of all quantized operations inside the block. As shown in Fig. 3(c), this Fisher-based score is also empirically predictive of the measured quantization loss, with Pearson correlation $r = 0.88$.

Diagonal approximation. Although the Fisher surrogate avoids second-order derivatives, the full matrix $\mathbf{F}_k^{h_l}$ is still a $C \times C$ matrix for each block and task. This is costly to store and its off-diagonal entries can be hard to estimate from a small calibration set. We therefore use the diagonal empirical Fisher:

$$F_k[l, c] = \mathbb{E}_{(x,y) \sim \mathcal{D}_{\text{cal}}} \left[\left(\frac{\partial \mathcal{L}_k(x, y)}{\partial h_{l,c}(x)} \right)^2 \right] \approx \frac{1}{N} \sum_{n=1}^N \left(\frac{\partial \mathcal{L}_k(x_n, y_n)}{\partial h_{l,c}(x_n)} \right)^2. \quad (8)$$

This reduces storage from $\mathcal{O}(C^2)$ to $\mathcal{O}(C)$. The quantity $F_k[l, c]$ is the second moment of the per-sample gradient on channel c . Under the population Fisher identity, where the expected score is

zero, it also equals the gradient variance. Keeping only the diagonal discards cross-channel terms and treats channel perturbations as locally independent. This approximation is sufficient for our goal, since we use the score to rank channel importance rather than to recover the full curvature matrix.

With this approximation, Eq. 7 becomes

$$\mathbb{E}[\Delta\mathcal{L}_k] \approx \frac{1}{2} \mathbb{E}_{x \sim \mathcal{D}_{\text{cal}}} \left[\sum_{c=1}^C F_k[l, c] (\Delta h_{l,c}(x))^2 \right]. \quad (9)$$

Thus, the loss increase is approximated by a channel-wise weighted reconstruction error at the block output. Each $F_k[l, c]$ measures how sensitive task k is to squared error on channel c of block l . Compared with a uniform reconstruction loss, this form assigns larger weights to channels that are more important for the task. We use these task-aware channel weights in the learnable affine transformation described next.

3.2.3 Integrating Fisher Information into Learnable Affine Transformations

Building on the per-channel Fisher score $F_k[l, c]$ from Section 3.2.2, we use task sensitivity to guide the calibration of learnable affine transformations. Let $l \in \{1, \dots, L\}$ index the calibrated transformer blocks, $c \in \{1, \dots, C\}$ index hidden channels, and $k \in \{1, \dots, K\}$ index VGGT task heads.

Block-wise calibration objective. Learnable affine transformation methods [Liu et al., 2024, Sun et al., 2025b] insert an invertible matrix \mathbf{P}_l into a linear layer and fold its inverse into the weight:

$$\mathbf{Y}_l = (\mathbf{X}_l \mathbf{P}_l) (\mathbf{P}_l^{-1} \mathbf{W}_l) = \mathbf{X}_l \mathbf{W}_l. \quad (10)$$

Quantization is then applied to the transformed activation $\mathbf{X}_l \mathbf{P}_l$ and transformed weight $\mathbf{P}_l^{-1} \mathbf{W}_l$, whose distributions are easier to quantize while preserving the full-precision computation before quantization.

For block l , standard calibration optimizes the learnable parameters θ_l by matching the quantized block output $\tilde{\mathbf{h}}_l$ to the full-precision output \mathbf{h}_l :

$$\mathcal{L}_{\text{uni}}^l(\theta_l) = \mathbb{E}_x \left[\frac{1}{|\mathcal{T}_l|C} \sum_{t \in \mathcal{T}_l} \sum_{c=1}^C (h_{l,t,c}(x) - \tilde{h}_{l,t,c}(x; \theta_l))^2 \right], \quad (11)$$

where \mathcal{T}_l denotes the tokens of block l . This uniform loss weights all channels equally, although errors in different channels can have very different effects on downstream task predictions.

Task-aware Fisher aggregation. VGGT predicts multiple tasks, and each task head gives a Fisher score $F_k[l, c]$ for channel c in block l . Since raw gradient magnitudes can differ across task heads, we first normalize each task by its mean Fisher value:

$$\bar{F}_k = \frac{1}{LC} \sum_{l'=1}^L \sum_{c'=1}^C F_k[l', c']. \quad (12)$$

We then combine the normalized scores with equal task weights:

$$s[l, c] = \sum_{k=1}^K \frac{F_k[l, c]}{\bar{F}_k}. \quad (13)$$

Here, L is the number of calibrated blocks and C is the hidden channel dimension. This normalization prevents a task with larger raw gradients from dominating the calibration weights.

Per-block normalization. Because calibration is performed block by block, we normalize the combined score within each block:

$$w_l[c] = \frac{s[l, c]}{\frac{1}{C} \sum_{c'=1}^C s[l, c']}. \quad (14)$$

Thus, each block has mean weight 1, so the loss scale is comparable across blocks. We also apply a small floor

$$w_l[c] \leftarrow \max(w_l[c], 0.01), \quad (15)$$

which prevents low-Fisher channels from being completely ignored.

Table 1: Camera pose estimation results for VGGT on Co3Dv2 [Reizenstein et al., 2021] and Re10K [Zhou et al., 2018]. AUC metrics measure the area under the cumulative error curve at different thresholds (higher is better). Best results in **bold**.

Method	Bitwidth (W/A)	Co3Dv2				Re10K			
		AUC@30 \uparrow	AUC@15 \uparrow	AUC@5 \uparrow	AUC@3 \uparrow	AUC@30 \uparrow	AUC@15 \uparrow	AUC@5 \uparrow	AUC@3 \uparrow
FP16	16/16	0.9731	0.9462	0.8462	0.7630	0.8667	0.7818	0.5803	0.4688
RTN	4/8	0.9619	0.9238	0.7822	0.6691	0.8483	0.7514	0.5318	0.4158
QuaRot	4/8	0.9672	0.9343	0.8098	0.7032	0.8480	0.7537	0.5307	0.4038
FlatQuant	4/8	0.9674	0.9351	0.8051	0.7191	0.8481	0.7543	0.5262	0.3958
QuantVGGT	4/8	0.9684	0.9363	0.8127	0.7117	0.8516	0.7587	0.5379	0.4125
FGQ	4/8	0.9686	0.9371	0.8185	0.7230	0.8566	0.7651	0.5485	0.4318
RTN	4/4	0.6547	0.3950	0.0474	0.0123	0.4334	0.2520	0.0590	0.0224
QuaRot	4/4	0.8169	0.6471	0.2252	0.0904	0.5722	0.3952	0.1381	0.0663
FlatQuant	4/4	0.9295	0.8648	0.6405	0.4691	0.7240	0.5849	0.3233	0.2169
QuantVGGT	4/4	0.9387	0.8840	0.6973	0.5419	0.7703	0.6437	0.3845	0.2710
FGQ	4/4	0.9425	0.8887	0.7025	0.5575	0.7704	0.6443	0.3898	0.2756

Fisher-guided calibration loss. **FGQ** replaces the uniform calibration loss with a Fisher-weighted objective:

$$\mathcal{L}_{\text{FGQ}}^l(\theta_l) = \mathbb{E}_x \left[\frac{1}{|\mathcal{T}_l|C} \sum_{t \in \mathcal{T}_l} \sum_{c=1}^C w_l[c] (h_{l,t,c}(x) - \tilde{h}_{l,t,c}(x; \theta_l))^2 \right]. \quad (16)$$

This objective allocates more calibration capacity to channels whose errors are more likely to affect VGGT task outputs, while still preserving all channels through the floor term.

4 Evaluation

4.1 Experimental Setup

Evaluation settings. We primarily evaluate **FGQ** on the open-source VGGT-1.2B model [Wang et al., 2025a]. We consider the main 3D vision tasks supported by VGGT and evaluate each task on standard benchmarks: (i) **camera pose estimation** on Co3Dv2 [Reizenstein et al., 2021] and Re10K [Zhou et al., 2018]; (ii) **point map reconstruction** on 7-Scenes [Shotton et al., 2013], DTU [Jensen et al., 2014], and ETH3D [Schops et al., 2017]; and (iii) **depth estimation** on KITTI [Geiger et al., 2013] for both monocular depth and video depth settings.

For the learnable affine quantization scheme, we implement **FGQ** on top of FlatQuant [Sun et al., 2025b]. FlatQuant is used as a strong and public quantization backbone, while **FGQ** elaborates the calibration objective. Detailed quantization and calibration settings are provided in Appendix B. We report results under both **W4A8** and **W4A4** settings to evaluate **FGQ** under different quantization regimes. To further test generalization, we also extend **FGQ** to the π^3 model [Wang et al., 2025b]. The result can be found in Appendix D.

Baselines. We compare **FGQ** against representative PTQ methods: (i) **RTN**: round-to-nearest quantization without calibration, serving as a lower bound; (ii) **QuaRot** [Ashkboos et al., 2024]: fixed Hadamard rotation for activation smoothing; (iii) **FlatQuant** [Sun et al., 2025b]: learnable affine transformations with uniform reconstruction loss, which serves as our base method; (iv) **QuantVGGT** [Feng et al., 2025]: a recent VGGT-specific PTQ method that addresses activation outliers from special tokens. For fair comparison, all methods use the same calibration set and quantization configuration.

4.2 Main Results

Camera pose estimation. Table 1 evaluates camera pose estimation on Co3Dv2 and Re10K. Under W4A8, most methods remain close to FP16, indicating that this task is relatively robust to moderate activation quantization. In this setting, **FGQ** still gives the best overall results on Re10K and competitive results on Co3Dv2. In the more challenging W4A4 setting, where activation quantization introduces a larger performance drop, **FGQ** consistently performs on par with or better than existing quantization baselines across datasets. Compared with the dense reconstruction results below, the

Table 2: Point map reconstruction results for VGGT on 7-Scenes [Shotton et al., 2013] and ETH3D [Schops et al., 2017]. Acc measures accuracy (higher is better), Comp measures completeness (lower is better), and N.C. measures normal consistency (higher is better). Best results in **bold**.

Method	Bitwidth (W/A)	7-Scenes						ETH3D					
		Acc.↓		Comp.↓		N.C.↑		Acc.↓		Comp.↓		N.C.↑	
		mean	med	mean	med	mean	med	mean	med	mean	med	mean	med
FP16	16/16	0.044	0.024	0.056	0.033	0.733	0.846	0.263	0.167	0.288	0.167	0.846	0.947
RTN	4/8	0.046	0.027	0.060	0.037	0.729	0.839	0.271	0.183	0.299	0.174	0.840	0.938
QuaRot	4/8	0.047	0.027	0.056	0.033	0.736	0.848	0.262	0.174	0.272	0.161	0.846	0.951
FlatQuant	4/8	0.045	0.025	0.055	0.031	0.732	0.845	0.262	0.169	0.287	0.168	0.845	0.943
QuantVGGT	4/8	0.044	0.025	0.056	0.033	0.729	0.840	0.269	0.185	0.292	0.170	0.842	0.942
FGQ	4/8	0.043	0.024	0.055	0.031	0.736	0.848	0.260	0.165	0.270	0.158	0.848	0.949
RTN	4/4	0.146	0.103	0.134	0.086	0.600	0.655	0.944	0.843	1.339	0.920	0.603	0.656
QuaRot	4/4	0.107	0.079	0.165	0.128	0.663	0.749	0.917	0.781	1.151	0.757	0.667	0.753
FlatQuant	4/4	0.056	0.036	0.070	0.047	0.717	0.824	0.291	0.193	0.297	0.173	0.833	0.935
QuantVGGT	4/4	0.053	0.032	0.085	0.059	0.719	0.828	0.312	0.206	0.305	0.180	0.832	0.937
FGQ	4/4	0.048	0.031	0.059	0.036	0.723	0.832	0.275	0.177	0.279	0.164	0.834	0.940

improvement on pose estimation is modest, suggesting that this global prediction task is less sensitive to the Fisher-guided channel selection than dense geometric outputs.

Point map reconstruction. Table 2 and 3 report point map reconstruction results on 7-Scenes, ETH3D, and DTU. **FGQ** shows a clearer advantage on this task. Point maps are dense geometric outputs, so activation quantization errors affect many spatial locations and can directly degrade surface accuracy, completeness, and normal consistency. Under W4A8, **FGQ** closely matches FP16 and obtains the strongest overall performance. Under W4A4, the advantage becomes more pronounced. On 7-Scenes, **FGQ** reduces the mean completeness error from 0.085 to 0.059 compared with QuantVGGT, while also improving mean accuracy from 0.053 to 0.048. On ETH3D, **FGQ** improves mean accuracy from 0.312 to 0.275 and mean completeness from 0.305 to 0.279. On DTU, **FGQ** also gives the best completeness and normal consistency among W4A4 methods. These results indicate that **FGQ** better preserves the features needed for dense 3D geometry. Qualitative comparisons are shown in Figure 1 and Appendix G. On 7-Scenes, **FGQ** (W4A4) preserves finer structural details than QuantVGGT (W4A4), while on DTU the QuantVGGT (W4A4) reconstruction appears visibly blurry and **FGQ** (W4A4) remains sharp.

Depth estimation. Table 4 reports depth estimation results on KITTI for both monocular and video inputs. **FGQ** consistently outperforms the quantization baselines in the W4A8 setting, achieving the best results across all metrics on both evaluation protocols. The gains are especially clear on error metrics such as AbsRel, SqRel, and RMSE, showing that Fisher-guided calibration better preserves the dense depth structure under activation quantization. In the more aggressive W4A4 setting, **FGQ** remains the strongest overall method. It achieves the best AbsRel, SqRel, and threshold accuracy on KITTI Mono, and the best overall error metrics on KITTI Video among the W4A4 methods. These results are consistent with the point map reconstruction experiments: **FGQ** provides larger benefits on dense geometric tasks than on global pose estimation, since dense outputs are more sensitive to spatially accumulated quantization errors.

Table 3: Point map reconstruction for VGGT on DTU [Jensen et al., 2014]. Best results in **bold**.

Method	Bitwidth (W/A)	DTU					
		Acc.↓		Comp.↓		N.C.↑	
		Mean	Med	Mean	Med	Mean	Med
FP16	16	1.308	0.761	1.929	1.015	0.665	0.750
RTN	4/8	1.363	0.786	1.904	0.976	0.669	0.753
QuaRot	4/8	1.401	0.815	1.899	0.978	0.668	0.754
FlatQuant	4/8	1.429	0.840	1.910	0.977	0.665	0.752
QuantVGGT	4/8	1.292	0.752	1.944	1.007	0.667	0.753
FGQ	4/8	1.287	0.742	1.881	0.965	0.675	0.762
RTN	4/4	7.987	5.648	4.355	2.593	0.657	0.731
QuaRot	4/4	3.470	2.107	2.145	1.077	0.665	0.750
FlatQuant	4/4	1.478	0.829	1.895	0.982	0.667	0.754
QuantVGGT	4/4	1.488	0.837	1.933	1.001	0.669	0.756
FGQ	4/4	1.420	0.801	1.879	0.965	0.669	0.757

It achieves the best AbsRel, SqRel, and threshold accuracy on KITTI Mono, and the best overall error metrics on KITTI Video among the W4A4 methods. These results are consistent with the point map reconstruction experiments: **FGQ** provides larger benefits on dense geometric tasks than on global pose estimation, since dense outputs are more sensitive to spatially accumulated quantization errors.

Table 4: Depth estimation results on KITTI (monocular and video depth). Lower is better for AbsRel, SqRel, and RMSE; higher is better for $\delta < 1.25$. Best results in **bold**.

Method	Bitwidth (W/A)	KITTI (Mono)				KITTI (Video)			
		AbsRel↓	SqRel↓	RMSE↓	$\delta < 1.25$ ↑	AbsRel↓	SqRel↓	RMSE↓	$\delta < 1.25$ ↑
FP16	16/16	0.092	0.459	3.902	0.936	0.058	0.373	3.618	0.961
RTN	4/8	0.093	0.453	3.903	0.936	0.058	0.348	3.500	0.964
QuaRot	4/8	0.087	0.443	3.897	0.943	0.059	0.364	3.642	0.963
FlatQuant	4/8	0.087	0.410	3.623	0.946	0.052	0.314	3.350	0.968
QuantVGGT	4/8	0.091	0.462	3.931	0.936	0.054	0.339	3.450	0.967
FGQ	4/8	0.086	0.396	3.566	0.947	0.051	0.292	3.240	0.970
RTN	4/4	0.148	0.728	5.159	0.823	0.164	0.985	5.615	0.748
QuaRot	4/4	0.117	0.487	4.083	0.903	0.126	0.713	4.896	0.838
FlatQuant	4/4	0.084	0.399	3.650	0.948	0.062	0.339	3.488	0.960
QuantVGGT	4/4	0.088	0.446	3.842	0.938	0.058	0.336	3.486	0.963
FGQ	4/4	0.079	0.389	3.642	0.951	0.056	0.313	3.384	0.965

Table 5: Ablation study on the Fisher Information design.

Fisher Info.	Co3Dv2 AUC@15 ↑	Fisher Info.	DTU Acc. mean ↓
plain (w/o Fisher)	0.8825	plain (w/o Fisher)	1.537
point	0.8868	camera	1.465
point + depth	0.8875	camera + depth	1.458
point + depth + camera	0.8952	camera + depth + point	1.446

4.3 Ablation study

We study the effect of different task losses in the empirical Fisher estimation. All variants use the same quantization setting, calibration data, optimization steps, and evaluation protocol. The plain baseline removes Fisher weighting and uses an unweighted calibration objective. Co3Dv2 mainly evaluates camera pose accuracy, while DTU evaluates point-map reconstruction. As shown in Table 5, Fisher weighting improves both benchmarks. On Co3Dv2, adding point and depth Fisher improves AUC@15 from 0.8825 to 0.8875, while further adding camera Fisher gives the largest gain and reaches 0.8952. On DTU, adding point Fisher to the camera-depth Fisher gives the best Acc. mean, reducing it from 1.458 to 1.446. This shows that the Fisher term is most useful when it includes the task aligned with the evaluation metric. At the same time, the gains from multi-task Fisher suggest that different task losses provide complementary channel sensitivity signals.

4.4 Efficiency Analysis

We evaluate the runtime efficiency of our W4A4 quantized model on a single NVIDIA A100 40G GPU. To measure the benefit of real low-bit execution, we use fake quantization as the baseline and report speedups from the real quantized implementation. Our implementation builds on the Triton kernel from FlatQuant [Sun et al., 2025b] and tailors it to our design. We decompose the latency into parameter loading and compute kernel time, where the compute kernel includes the affine transformation, quantization, and quantized linear computation. For parameter loading, RTN and our method achieve similar speedups, $3.41\times$ and $3.42\times$, since both benefit from 4-bit weight and activation storage. For the compute kernel, RTN reaches $6.01\times$, while our method reaches $4.67\times$. The gap comes from the extra affine transformation used by our method. At the full block level, RTN obtains $2.01\times$ speedup and our method still achieves $1.81\times$ speedup. These results show that our method keeps most of the real quantization efficiency while adding only moderate runtime overhead for the accuracy-preserving affine transformation.

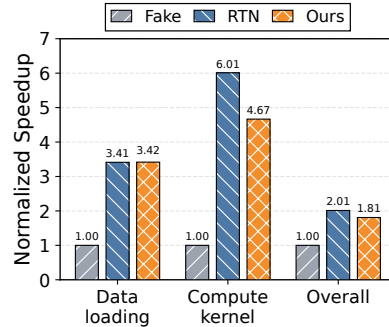


Figure 4: Normalized Speedup over the same W4A4 quantization settings.

5 Conclusion

We presented Fisher-Guided Quantization (**FGQ**), a post-training quantization method for feed-forward 3D reconstruction models. Our main observation is that different transformer blocks and hidden channels in the model contribute differently to each task. As a result, uniformly treating all outputs during calibration can therefore preserve insensitive tasks while harming the tasks that are more sensitive to quantization noise. **FGQ** addresses this issue by using diagonal Fisher information to estimate task-aware block and channel sensitivities, and by incorporating these sensitivities into the learnable affine transformation during calibration. Extensive experiments show that **FGQ** consistently outperforms existing PTQ baselines under 4-bit quantization, with the largest gains appearing on point map reconstruction, where prior PTQ methods suffer the most severe degradation.

References

- Saleh Ashkboos, Amirkeivan Mohtashami, Maximilian L Croci, Bo Li, Pashmina Cameron, Martin Jaggi, Dan Alistarh, Torsten Hoefler, and James Hensman. Quarot: Outlier-free 4-bit inference in rotated llms. *Advances in Neural Information Processing Systems*, 37:100213–100240, 2024.
- Weilun Feng, Haotong Qin, Mingqiang Wu, Chuanguang Yang, Yuqi Li, Xiangqi Li, Zhulin An, Libo Huang, Yulun Zhang, Michele Magno, et al. Quantized visual geometry grounded transformer. *arXiv preprint arXiv:2509.21302*, 2025.
- Elias Frantar, Saleh Ashkboos, Torsten Hoefler, and Dan Alistarh. Gptq: Accurate post-training quantization for generative pre-trained transformers. *arXiv preprint arXiv:2210.17323*, 2022.
- Andreas Geiger, Philip Lenz, Christoph Stiller, and Raquel Urtasun. Vision meets robotics: The kitti dataset. *The international journal of robotics research*, 32(11):1231–1237, 2013.
- Wenbo Hu, Jingli Lin, Yilin Long, Yunlong Ran, Lihan Jiang, Yifan Wang, Chenming Zhu, Runsen Xu, Tai Wang, and Jiangmiao Pang. g^2 vlm: Geometry grounded vision language model with unified 3d reconstruction and spatial reasoning. *arXiv preprint arXiv:2511.21688*, 2025.
- Rasmus Jensen, Anders Dahl, George Vogiatzis, Engin Tola, and Henrik Aanæs. Large scale multi-view stereopsis evaluation. In *Proceedings of the IEEE conference on computer vision and pattern recognition*, pages 406–413, 2014.
- Woosuk Kwon, Sehoon Kim, Michael W Mahoney, Joseph Hassoun, Kurt Keutzer, and Amir Gholami. A fast post-training pruning framework for transformers. *Advances in Neural Information Processing Systems*, 35:24101–24116, 2022.
- Yann LeCun, John Denker, and Sara Solla. Optimal brain damage. *Advances in neural information processing systems*, 2, 1989.
- Ji Lin, Jiaming Tang, Haotian Tang, Shang Yang, Wei-Ming Chen, Wei-Chen Wang, Guangxuan Xiao, Xingyu Dang, Chuang Gan, and Song Han. Awq: Activation-aware weight quantization for on-device llm compression and acceleration. *Proceedings of machine learning and systems*, 6: 87–100, 2024.
- Junhong Lin, Kangli Wang, Shunzhou Wang, Songlin Fan, Ge Li, and Wei Gao. Vgd: Visual geometry gaussian splatting for feed-forward surround-view driving reconstruction. *arXiv preprint arXiv:2510.19578*, 2025.
- Zechun Liu, Changsheng Zhao, Igor Fedorov, Bilge Soran, Dhruv Choudhary, Raghuraman Krishnamoorthi, Vikas Chandra, Yuandong Tian, and Tijmen Blankevoort. Spinqant: Llm quantization with learned rotations. *arXiv preprint arXiv:2405.16406*, 2024.
- Maxime Oquab, Timothée Darcet, Théo Moutakanni, Huy Vo, Marc Szafraniec, Vasil Khalidov, Pierre Fernandez, Daniel Haziza, Francisco Massa, Alaaeldin El-Nouby, et al. Dinov2: Learning robust visual features without supervision. *arXiv preprint arXiv:2304.07193*, 2023.
- Sicheng Pan, Chen Tang, Shuzhao Xie, Ke Yang, Weixiang Zhang, Jiawei Li, Bin Chen, Shu-Tao Xia, and Zhi Wang. Tail-aware post-training quantization for 3d geometry models. *arXiv preprint arXiv:2602.01741*, 2026.

- Jeremy Reizenstein, Roman Shapovalov, Philipp Henzler, Luca Sbordon, Patrick Labatut, and David Novotny. Common objects in 3d: Large-scale learning and evaluation of real-life 3d category reconstruction. In *Proceedings of the IEEE/CVF international conference on computer vision*, pages 10901–10911, 2021.
- Thomas Schops, Johannes L Schonberger, Silvano Galliani, Torsten Sattler, Konrad Schindler, Marc Pollefeys, and Andreas Geiger. A multi-view stereo benchmark with high-resolution images and multi-camera videos. In *Proceedings of the IEEE conference on computer vision and pattern recognition*, pages 3260–3269, 2017.
- You Shen, Zhipeng Zhang, Yansong Qu, Xiawu Zheng, Jiayi Ji, Shengchuan Zhang, and Lijuan Cao. Fastvggt: Training-free acceleration of visual geometry transformer. *arXiv preprint arXiv:2509.02560*, 2025.
- Jamie Shotton, Ben Glocker, Christopher Zach, Shahram Izadi, Antonio Criminisi, and Andrew Fitzgibbon. Scene coordinate regression forests for camera relocalization in rgb-d images. In *Proceedings of the IEEE conference on computer vision and pattern recognition*, pages 2930–2937, 2013.
- Zhijian Shu, Cheng Lin, Tao Xie, Wei Yin, Ben Li, Zhiyuan Pu, Weize Li, Yao Yao, Xun Cao, Xiaoyang Guo, et al. Litevggt: Boosting vanilla vgggt via geometry-aware cached token merging. *arXiv preprint arXiv:2512.04939*, 2025.
- Xianbing Sun, Zhikai Zhu, Zhengyu Lou, Bo Yang, Jinyang Tang, Liqing Zhang, He Wang, and Jianfu Zhang. Avggt: Rethinking global attention for accelerating vgggt. *arXiv preprint arXiv:2512.02541*, 2025a.
- Yuxuan Sun, Ruikang Liu, Haoli Bai, Han Bao, Kang Zhao, Yuening Li, Jiaxin Hu, Xianzhi Yu, Lu Hou, Chun Yuan, et al. Flatquant: Flatness matters for llm quantization. In *International Conference on Machine Learning*, pages 57587–57613. PMLR, 2025b.
- Jianyuan Wang, Minghao Chen, Nikita Karaev, Andrea Vedaldi, Christian Rupprecht, and David Novotny. Vgggt: Visual geometry grounded transformer. In *Proceedings of the Computer Vision and Pattern Recognition Conference*, pages 5294–5306, 2025a.
- Yifan Wang, Jianjun Zhou, Haoyi Zhu, Wenzheng Chang, Yang Zhou, Zizun Li, Junyi Chen, Jiangmiao Pang, Chunhua Shen, and Tong He. π^3 : Permutation-equivariant visual geometry learning. *arXiv preprint arXiv:2507.13347*, 2025b.
- Zipeng Wang and Dan Xu. Flashvggt: Efficient and scalable visual geometry transformers with compressed descriptor attention. *arXiv preprint arXiv:2512.01540*, 2025.
- Huanrui Yang, Yafeng Huang, Zhen Dong, Denis A Gudovskiy, Tomoyuki Okuno, Yohei Nakata, Yuan Du, Kurt Keutzer, and Shanghang Zhang. Fisher-aware quantization for detr detectors with critical-category objectives. *arXiv preprint arXiv:2407.03442*, 2024.
- Sizhe Yang, Linning Xu, Hao Li, Juncheng Mu, Jia Zeng, Dahua Lin, and Jiangmiao Pang. Robo3r: Enhancing robotic manipulation with accurate feed-forward 3d reconstruction. *arXiv preprint arXiv:2602.10101*, 2026.
- Yipu Zhang, Jintao Cheng, Xingyu Liu, Zeyu Li, Carol Jingyi Li, Jin Wu, Lin Jiang, Yuan Xie, Jiang Xu, and Wei Zhang. Versaq-3d: A reconfigurable accelerator enabling feed-forward and generalizable 3d reconstruction via versatile quantization. *arXiv preprint arXiv:2601.20317*, 2026.
- Tinghui Zhou, Richard Tucker, John Flynn, Graham Fyffe, and Noah Snavely. Stereo magnification: Learning view synthesis using multiplane images. *arXiv preprint arXiv:1805.09817*, 2018.

A Proof of Proposition 3.1

We prove the identity for a continuous label space. The same argument applies to discrete labels by replacing integrals with sums. Fix an input x . Since $p_z(y | x)$ is a normalized conditional distribution,

$$\int p_z(y | x) dy = 1. \quad (17)$$

Under the stated regularity conditions, we may differentiate Eq. (17) with respect to z . Differentiating once gives

$$0 = \int \nabla_z p_z(y | x) dy = \int p_z(y | x) \nabla_z \log p_z(y | x) dy. \quad (18)$$

Thus the expected score is zero:

$$\mathbb{E}_{y \sim p_z(\cdot | x)} [\nabla_z \log p_z(y | x)] = 0. \quad (19)$$

Differentiating Eq. (18) once more gives

$$\begin{aligned} 0 &= \int \nabla_z [p_z(y | x) \nabla_z \log p_z(y | x)] dy \\ &= \int p_z(y | x) [\nabla_z^2 \log p_z(y | x) + \nabla_z \log p_z(y | x) \nabla_z \log p_z(y | x)^\top] dy. \end{aligned} \quad (20)$$

Equivalently,

$$\mathbb{E}_{y \sim p_z(\cdot | x)} [-\nabla_z^2 \log p_z(y | x)] = \mathbb{E}_{y \sim p_z(\cdot | x)} [\nabla_z \log p_z(y | x) \nabla_z \log p_z(y | x)^\top]. \quad (21)$$

Now define the negative log-likelihood loss

$$\ell(z; x, y) = -\log p_z(y | x). \quad (22)$$

Then

$$\nabla_z^2 \ell(z; x, y) = -\nabla_z^2 \log p_z(y | x), \quad \nabla_z \ell(z; x, y) = -\nabla_z \log p_z(y | x). \quad (23)$$

Substituting these relations into Eq. (21) yields

$$\mathbb{E}_{y \sim p_z(\cdot | x)} [\nabla_z^2 \ell(z; x, y)] = \mathbb{E}_{y \sim p_z(\cdot | x)} [\nabla_z \ell(z; x, y) \nabla_z \ell(z; x, y)^\top]. \quad (24)$$

Evaluating Eq. (24) at $z = z^*$ and using the assumption $q(y | x) = p_{z^*}(y | x)$, we obtain

$$\mathbb{E}_{y \sim q(\cdot | x)} [\nabla_z^2 \ell(z^*; x, y)] = \mathbb{E}_{y \sim q(\cdot | x)} [\nabla_z \ell(z^*; x, y) \nabla_z \ell(z^*; x, y)^\top]. \quad (25)$$

Finally, taking expectation over $x \sim q(x)$ gives

$$\mathbb{E}_{x \sim q(x), y \sim q(y | x)} [\nabla_z^2 \ell(z^*; x, y)] = \mathbb{E}_{x \sim q(x), y \sim q(y | x)} [\nabla_z \ell(z^*; x, y) \nabla_z \ell(z^*; x, y)^\top], \quad (26)$$

which proves Proposition 3.1. \square

B Quantization and Calibration Settings

Implementation based on FlatQuant. FGQ is implemented on top of FlatQuant [Sun et al., 2025b]. We use the same learnable affine transformation modules, learnable clipping parameters, and quantizer placement as FlatQuant. All pretrained model parameters are frozen before calibration. Calibration is performed block by block, and only the calibration parameters in the current block are optimized. Specifically, the trainable parameters are the FlatQuant transformation parameters, including the transformation matrices and diagonal scales, together with the learnable weight-clipping and activation-clipping factors. The original linear weights and biases, normalization layers, patch embedding/DINOv2 backbone, prediction heads, and all non-current blocks are kept frozen. This setup isolates the effect of replacing the standard FlatQuant reconstruction loss with the proposed Fisher-guided calibration loss.

Quantization setting. For the default W4A4 setting, both weights and activations are quantized to 4 bits. Weight and activation quantization are symmetric. Weights are quantized per output channel, while activations are quantized per token without grouping. Learnable weight clipping and learnable activation clipping are enabled. Quantization is applied to the attention projections, including Q , K , V , and output projections, as well as the MLP linear layers in the VGGT aggregator frame and global blocks. The DINOv2/patch embedding module, camera/depth/point/track heads, normalization parameters, and special tokens are not quantized.

Tasks and metrics. VGGT jointly predicts three tasks. For **depth estimation**, we report absolute relative error (AbsRel) and δ_1 accuracy (percentage of pixels with relative error < 1.25). For **camera pose estimation**, we report the Area Under the Curve (AUC) of pose accuracy across multiple thresholds. For **point map reconstruction**, we report Accuracy (Acc.), Completeness (Comp.), and Normal Consistency (N.C.), with both mean and median values.

Calibration data. We use Co3Dv2 [Reizenstein et al., 2021] as the calibration data source. For calibration, we sample 64 clips, with 4 frames per clip. The batch size is 2 clips, corresponding to 8 frames per mini-batch. The default random seed is 42. The sampled calibration clips are loaded once and then reused for all blocks and all calibration epochs. The implementation samples directly from the raw Co3Dv2 directory by first sampling a category, then a sequence, and then 4 images from the sequence image folder. The current sampler does not use annotation-based quality filters. Frames are randomly sampled from the available images in each sequence, and no explicit temporal stride or temporal ordering constraint is imposed.

Optimization hyperparameters. Calibration uses AdamW. Unless overridden by parameter groups, AdamW uses the PyTorch default hyperparameters: $\beta_1 = 0.9$, $\beta_2 = 0.999$, $\epsilon = 10^{-8}$, and weight decay 0.01. No gradient clipping is used. Mixed precision is enabled by default using CUDA bfloat16 autocast, without a gradient scaler. The base learning rate for the FlatQuant transformation matrices and diagonal scales is 10^{-2} . The learning rate for the learnable weight-clipping and activation-clipping factors is 10 times larger, i.e., 10^{-1} in the default W4A4 setting.

The learning rate is decayed with a cosine schedule. The scheduler is stepped once per optimizer step. For each block, the number of calibration epochs is 15. With 64 clips and a batch size of 2 clips, this gives 32 mini-batches per epoch and 480 optimizer steps per block. VGGT contains 48 calibrated aggregator blocks, so the full W4A4 calibration uses $48 \times 480 = 23040$ optimizer steps. The cosine schedule uses

$$T_{\max} = \text{epochs} \times (\text{nsamples} // \text{cali_bsz}),$$

with minimum learning rate $\eta_{\min} = 10^{-5}$ for the default setting.

Model mode during calibration. The model is kept in evaluation mode during calibration. Thus, dropout and stochastic-depth layers are disabled, and batch-normalization layers, if present, use evaluation behavior. Gradients are enabled only for the current block’s calibration parameters. For each block, the full-precision output of that block is first used as the reconstruction target, and the quantized block output is then optimized to match this target.

Fisher information estimation. For FGQ, the Fisher information is estimated once before calibration and then kept fixed throughout calibration. We use the same Co3Dv2 sampling configuration as calibration: 64 clips, 4 frames per clip, image size 518, and random seed 42. The Fisher-estimation clips and calibration clips are generated independently by the same deterministic sampling procedure, rather than being explicitly saved and reused by identity.

Our implementation uses a diagonal activation Fisher approximation rather than a parameter Fisher. Hooks are registered on the outputs of the VGGT aggregator frame and global blocks. For VGGT, this gives 48 calibrated blocks. We estimate Fisher information for three output tasks: camera, depth, and world points, corresponding to `pose_enc`, `depth`, and `world_points`. For each task, we use the sum of the task output as the scalar objective and accumulate squared gradients with respect to the hooked block activations. For task k , block ℓ , and channel c , the raw Fisher estimate is

$$F_{k,\ell,c} = \frac{1}{N} \sum_{n=1}^N \sum_t \left(\frac{\partial \mathcal{L}_k}{\partial h_{\ell,t,c}^{(n)}} \right)^2,$$

Table 6: Calibration overhead and end-task performance comparison. Numbers in red indicate the change of FGQ relative to the Baseline PTQ (FlatQuant).

Method	Calibration Overhead		Performance	
	GPU memory (GB)	GPU time (hours)	AUC@15 (Co3Dv2)↑	DTU Acc. mean↓
FP16	–	–	0.9462	1.308
Baseline PTQ (FlatQuant)	3.54	0.87	0.8825	1.537
FGQ (Ours)	3.62 _{+0.08}	0.92 _{+0.05}	0.8952 _{+0.0127}	1.446 _{-0.091}

where $h_{\ell,t,c}^{(n)}$ is the activation of channel c at token t in block ℓ for sample n , and \mathcal{L}_k is the scalar objective for task k . The Fisher tensor therefore has shape $3 \times 48 \times 1024$, corresponding to tasks, blocks, and channels. Forward passes for Fisher estimation use CUDA bfloat16 autocast, while gradients are cast to float32 before accumulation. The saved Fisher tensor is stored in float32.

Before being used in FGQ calibration, the raw Fisher tensor is normalized. First, each task Fisher is divided by its global mean. The normalized task Fishers are then summed with equal weight. Finally, the resulting per-block Fisher weights are normalized so that each block has mean weight 1, and the minimum weight is clamped to 0.01. No clipping or damping is applied to the raw Fisher values before this loading-time normalization.

FGQ calibration loss. FlatQuant uses an unweighted block-output reconstruction loss,

$$\mathcal{L}_{\text{FlatQuant}} = \text{MSE}(\mathbf{y}_{\ell}^q, \mathbf{y}_{\ell}^{\text{fp}}),$$

where \mathbf{y}_{ℓ}^q and $\mathbf{y}_{\ell}^{\text{fp}}$ denote the quantized and full-precision outputs of the current block ℓ , respectively. FGQ replaces this loss with a Fisher-weighted reconstruction loss,

$$\mathcal{L}_{\text{FGQ}} = \frac{1}{|\mathcal{T}|C} \sum_{t \in \mathcal{T}} \sum_{c=1}^C w_{\ell,c} \left(y_{\ell,t,c}^q - y_{\ell,t,c}^{\text{fp}} \right)^2,$$

where $w_{\ell,c}$ is the fixed Fisher-derived weight for channel c in block ℓ , \mathcal{T} is the set of tokens, and C is the channel dimension. Calibration proceeds block by block in the order

$$\text{frame_0, global_0, } \dots, \text{ frame_23, global_23.}$$

Before backpropagation, the scalar loss is divided by its detached value. This normalization preserves the gradient direction while stabilizing the gradient scale.

C Calibration Overhead

All calibration experiments are conducted on a single NVIDIA A100 40GB GPU. In a representative W4A4 run, FlatQuant takes 52.53 minutes for calibration, while FGQ takes 55.54 minutes. The corresponding peak GPU memory usage is 3.54 GB for FlatQuant and 3.62 GB for FGQ. Compared with FlatQuant, FGQ increases the calibration time by 3.01 minutes, corresponding to a relative overhead of approximately 5.73%, and increases the peak GPU memory usage by only 0.08 GB, corresponding to approximately 2.26%. Because Fisher estimation uses only 64 clips with 4 frames per clip and is performed once, its cost remains small compared with model training. The detailed calibration memory usage and computation time are given in Table 6.

D FGQ Evaluation Result on π^3

We further extend our method to π^3 [Wang et al., 2025b], the most recent feed-forward 3D reconstruction model. Table 7 summarizes FGQ’s performance on π^3 .

On camera pose estimation, RTN collapses under 4/4 quantization, with AUC@3 on Co3Dv2 dropping from 0.5140 (FP16) to 0.0246, showing that π^3 is highly sensitive to quantization error. FlatQuant recovers a large portion of this gap but still suffers noticeable degradation at tight thresholds such as AUC@5 and AUC@3. FGQ consistently improves over FlatQuant on every threshold of both

Table 7: π^3 [Wang et al., 2025b] evaluation results. Top: camera pose estimation on Co3Dv2 [Reizenstein et al., 2021] and Re10K [Zhou et al., 2018] (AUC, higher is better). Bottom: point map reconstruction on DTU [Jensen et al., 2014] and ETH3D [Schops et al., 2017] (Acc and Comp lower is better; N.C. higher is better). Best results in **bold**.

Method	Bitwidth (W/A)	Co3Dv2				Re10K			
		AUC@30 \uparrow	AUC@15 \uparrow	AUC@5 \uparrow	AUC@3 \uparrow	AUC@30 \uparrow	AUC@15 \uparrow	AUC@5 \uparrow	AUC@3 \uparrow
FP16	16/16	0.9441	0.8882	0.6811	0.5140	0.8907	0.8212	0.6511	0.5523
RTN	4/4	0.7684	0.5491	0.0954	0.0246	0.5662	0.4040	0.1538	0.0740
FlatQuant	4/4	0.9119	0.8240	0.5022	0.2686	0.8298	0.7317	0.5204	0.4142
FGQ	4/4	0.9394	0.8795	0.6711	0.5032	0.8436	0.7502	0.5517	0.4461

Method	Bitwidth (W/A)	DTU						ETH3D					
		Acc. \downarrow		Comp. \downarrow		N.C. \uparrow		Acc. \downarrow		Comp. \downarrow		N.C. \uparrow	
		mean	med	mean	med	mean	med	mean	med	mean	med	mean	med
FP16	16/16	1.138	0.606	1.926	0.624	0.662	0.747	0.188	0.123	0.211	0.128	0.884	0.971
RTN	4/4	7.744	5.814	19.290	17.076	0.585	0.630	1.353	1.263	2.030	1.647	0.589	0.628
FlatQuant	4/4	1.396	0.745	1.917	0.622	0.662	0.746	0.197	0.134	0.217	0.145	0.870	0.959
FGQ	4/4	1.358	0.726	1.878	0.599	0.663	0.747	0.193	0.130	0.215	0.131	0.874	0.961

Co3Dv2 and Re10K, with the largest gains observed at tighter thresholds. For example, on Co3Dv2 FGQ raises AUC@3 from 0.2686 (FlatQuant) to 0.5032, approaching the FP16 result of 0.5140.

For point map reconstruction, FGQ outperforms FlatQuant on all metrics across DTU and ETH3D, and its results closely track the FP16 baseline (e.g., DTU Acc. mean 1.358 vs. FP16’s 1.138, ETH3D N.C. mean 0.874 vs. FP16’s 0.884). Overall, these results demonstrate that FGQ preserves π^3 ’s 3D geometric reasoning quality under aggressive 4-bit quantization while incurring minimal calibration overhead.

E Limitations

FGQ has several limitations that we leave for future work. First, our experiments focus on standard INT4 weight-activation quantization. We have not yet studied how Fisher-guided calibration interacts with newer low-precision formats, such as MXFP4 or other floating-point 4-bit variants. Since these formats have different dynamic ranges and rounding behavior, they may benefit from different calibration schedules or Fisher weighting strategies.

Second, FGQ is evaluated with a fixed calibration protocol. We use the same calibration data scale and preprocessing across experiments to isolate the effect of Fisher-guided weighting. We do not attempt to optimize the calibration set construction, such as the category balance, scene diversity, or view distribution. Studying how to choose the most informative calibration samples for feed-forward 3D reconstruction is an interesting direction, but is orthogonal to the calibration objective proposed in this work.

F Impact Statement

This work advances the practical deployment of feed-forward 3D reconstruction models by substantially reducing their memory and computational overhead through post-training quantization, enabling on-device 3D perception for applications such as augmented and virtual reality, robotics, autonomous driving, and assistive technologies. By lowering hardware requirements, FGQ helps democratize access to advanced 3D vision capabilities for researchers and developers with limited resources, while also reducing the energy consumption and carbon footprint associated with running billion-parameter models.

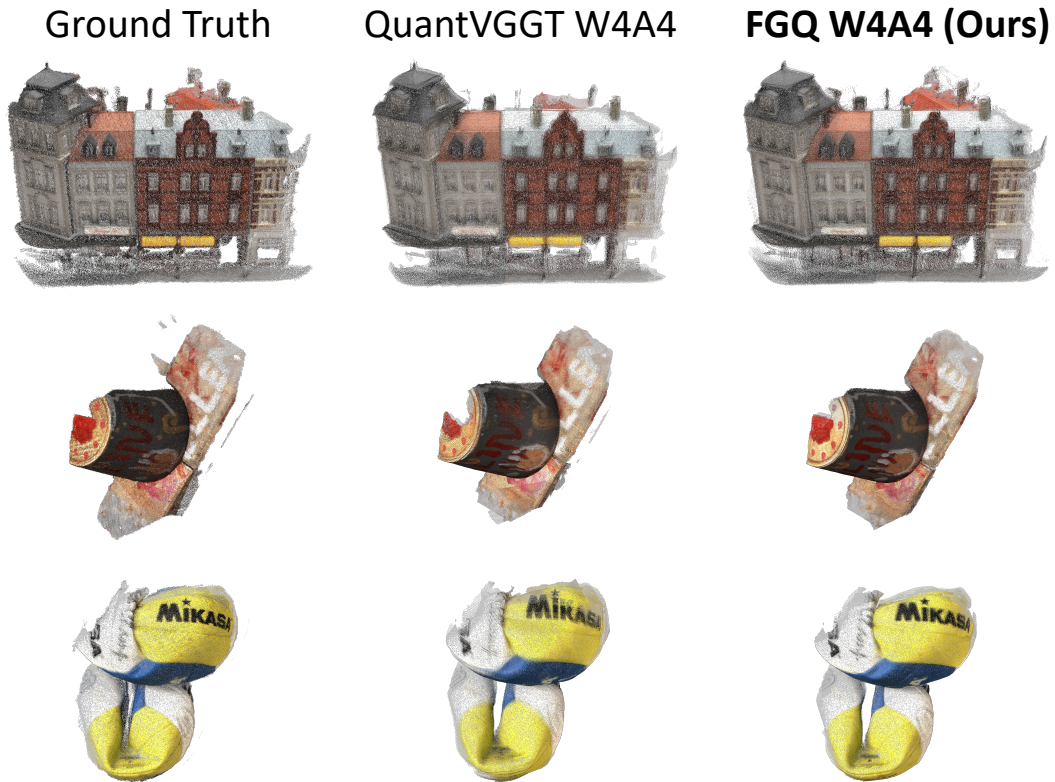


Figure 5: Visual comparison results for VGGT on DTU [Jensen et al., 2014] for Ground Truth, QuantVGGT [Feng et al., 2025] W4A4, and FGQ W4A4.

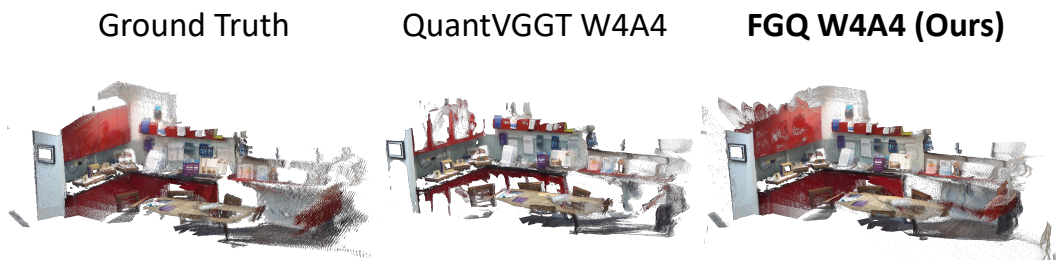


Figure 6: Visual comparison results for VGGT on 7-Scenes [Shotton et al., 2013] for Ground Truth, QuantVGGT [Feng et al., 2025] W4A4, and FGQ W4A4.

G More Visualization Results

Here we exhibit more visualization result for VGGT [Wang et al., 2025a] on DTU [Jensen et al., 2014] (Fig. 5) and 7-Scenes [Shotton et al., 2013] (Fig. 6).

Moreover, we provide the visualization result for π^3 [Wang et al., 2025b] on 7-Scenes [Shotton et al., 2013] in Fig. 7 to show FGQ’s improvement over RTN.

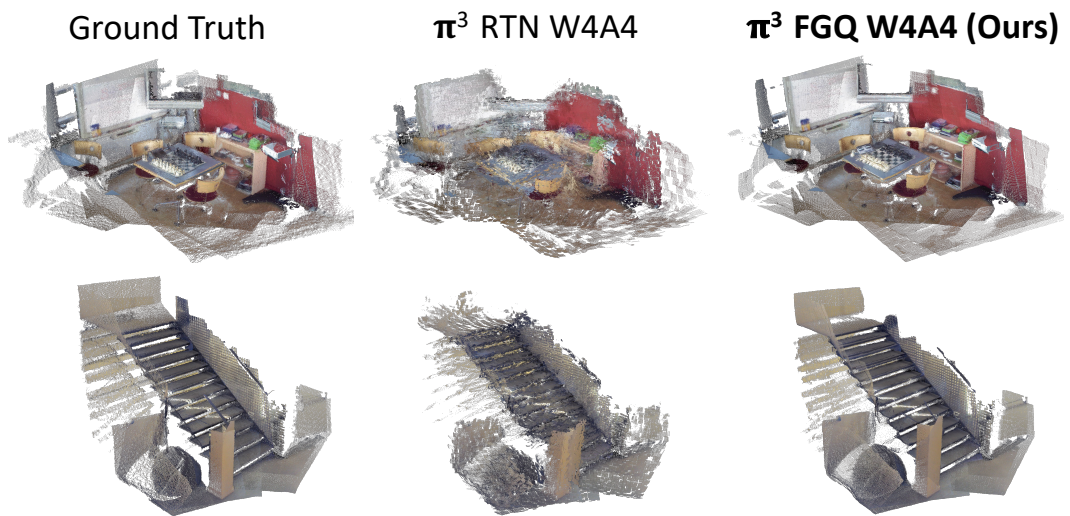


Figure 7: Visual comparison results for π^3 on 7-Scenes [Shotton et al., 2013] for Ground Truth, RTN W4A4, and FGQ W4A4.